

A free, open-source method for automated mapping of quantitative mineralogy from energy-dispersive X-ray spectroscopy scans of rock thin sections

Miles M. Reed¹, Ken L. Ferrier¹, William O. Nachlas¹, Bil Schneider¹, Chloé Arson², Tingting Xu³, Xianda Shen^{4,5}, and Nicole West⁶

¹ Geoscience, University of Wisconsin-Madison, United States

² Civil and Environmental Engineering, Cornell University, United States

³ Hopkins Extreme Materials Institute, John Hopkins University, United States

⁴ Key Laboratory of Geotechnical and Underground Engineering of Ministry of Education, Tongji University, China

⁵ Department of Geotechnical Engineering, Tongji University, China

⁶ Independent Researcher

Correspondence to: Miles Reed (miles.reed@wisc.edu)

Abstract

Quantitative mapping of minerals in rock thin sections delivers data on mineral abundance, size, and spatial arrangement that are useful for many geoscience and engineering disciplines. Although automated methods for mapping mineralogy exist, these are often expensive, associated with proprietary software, or require programming skills, which limits their usage. Here we present a free, open-source method for automated mineralogy mapping from energy dispersive spectroscopy (EDS) scans of rock thin sections. This method uses a random forest machine learning image classification algorithm within the QGIS geographic information system and Orfeo Toolbox, which are both free and open source. To demonstrate the utility of this method, we apply it to 14 rock thin sections from the well-studied Rio Blanco tonalite lithology of Puerto Rico. Measurements of mineral abundance inferred from our method compare favourably to previous measurements of mineral abundance inferred from X-ray diffraction and point counts on thin sections. The model-generated mineral maps agree with independent, manually-delineated mineral maps at a mean rate of 95%, with accuracies as high as 96% for the most abundant mineral (plagioclase) and as low as 72% for the least abundant mineral (apatite) in these samples. We show that the default random forest hyperparameters (i.e., tuneable settings that control behaviour) in Orfeo Toolbox yielded high accuracy in the model-generated mineral maps, and we demonstrate how users can determine the sensitivity of the mineral maps to hyperparameter values and input features. These results show that this method can be used to generate accurate maps of major minerals in rock thin sections using entirely free and open-source applications.

1 Introduction

33 Minerals are the fundamental units of rocks and many engineered materials (Perkins, 2020; Callister and
34 Rethwisch, 2020). Improving the quantification of mineral properties is a longstanding research objective in
35 industry and academic research (Pirrie and Rollinson, 2011), given the importance of mineral properties in
36 chemical weathering (e.g., Hilton and West, 2020), rock damage (e.g., Shen et al., 2019; Xu et al., 2022),
37 planetary evolution (e.g., Hazen et al., 2008), crustal deformation (e.g., Burgmann and Dresen, 2008), and
38 nutrient supply (e.g., Callahan et al., 2022). Quantitative automated mineralogy, the computerized mapping of
39 minerals across a sample, results in measurements of mineral modal abundance, mineral grain size and shape, and
40 the spatial arrangement of minerals amongst one another (Sutherland et al., 1988; Sutherland & Gottlieb, 1991;
41 Gu, 2003; Schulz et al., 2020). Modal abundance is useful because it can yield information on the sedimentary
42 and tectonic environments in which the rock formed (Harlov et al., 1998; Hupp and Donovan, 2018), while the
43 spatial arrangement of minerals in a rock, termed rock fabric, can yield further data on mechanical anisotropy and
44 paleo-environmental conditions during the rock's formation and metamorphism (Přikryl, 2006; Bjørlykke, 2014).
45 Simultaneous quantification of modal mineralogy and detailed mapping of the spatial arrangement of minerals in
46 an automated manner, or automated mineralogy, is thus a key tool for investigating many geologic processes.
47 Wide adoption of automated mineralogy techniques are limited by the prohibitive cost or programming skills
48 required to use many automated mineralogy software applications, so this technique has been mostly restricted to
49 ore characterization, resource processing, and petroleum geology (Nikonow and Rammlmair, 2017; Schulz et al.,
50 2020).

51

52 In practice, automated mineralogy methods use a combination of image analysis and classification methods to
53 identify minerals from elemental composition data (or their derivatives), which can be collected with a variety of
54 analytical methods, including energy dispersive X-ray spectroscopy (EDS), micro-X-ray fluorescence (μ -XRF),
55 and laser-induced breakdown spectroscopy (LIBS) (Nikonow et al., 2019). Automated mineralogy is being
56 slowly adopted by researchers outside of resource extraction for combined modal analysis of bulk mineralogy,
57 estimates of grain size distribution, and mineral association (Han et al., 2022), which can be useful in a variety of
58 disciplines such as petrology, applied geochemistry, and rock mechanics (Sajid et al., 2016; Elghali et al., 2018;
59 Rafiei et al., 2020).

60

61 Automated mineralogy from EDS with the aid of back-scattered electron (BSE) imaging has been developing
62 since the 1980s and has grown alongside advances in scanning electron microscopy (SEM) and image processing
63 algorithms (Miller et al., 1983; Fandrich et al., 2007). Commercial automated mineralogy systems are available

64 as integrated hardware-software systems or as standalone software packages which are combined with scanning
65 electron microscopes (Schulz et al., 2020). Some systems only work with certain scanning electron microscopes
66 and detectors from the same company QEMSCAN (Gottlieb et al., 2000), FEI-MLA (Fandrich et al., 2007), and
67 TESCAN TIMA-X (Hrstka et al., 2018). Others are purely software-based solutions which are integrated with
68 various SEMs: ZEISS Mineralogic, Oxford AZTecMineral, and Thermo-Scientific MAPS Mineralogy. The price
69 of hardware and software upgrades required to accommodate these systems renders them cost prohibitive to
70 many labs outside the resource extraction industry (Nikonow and Rammlmair, 2017). All systems have some
71 general ability to classify EDS spectra based on a database of pre-defined and/or customizable mineral spectra
72 standards (Schulz et al., 2020). Since the underlying software is proprietary, no source code is available for these
73 systems, and details on how they use spectra to classify minerals are sparse to non-existent (Kuelen et al., 2020).
74 Furthermore, the accuracy of mineral prediction from these systems has rarely been quantified (Blannin et al.,
75 2021).

76
77 To date, several open-source (i.e., source code is available and modifiable) automated mineralogy solutions have
78 been implemented. Ortolano et al. (2014, 2018) predicted modal mineralogy and mapped minerals from a
79 multistep workflow involving principal component analysis, maximum likelihood classification, and multi-linear
80 regression performed on EDS or WDS spectral data using the Python extension within ArcGIS. Li et al. (2021)
81 used a variety of legacy machine-learning and deep-learning models to classify minerals in oil reservoir rocks
82 using mineral maps generated from proprietary software as training data. In terms of image classification, deep-
83 learning methods are state of the art but currently require the user to be relatively adept at programming and
84 knowledgeable of the computer vision principles employed (Khan et al., 2018; Zhang et al., 2019). A method that
85 requires little to no programming ability would allow more users to benefit from automated mineralogy data. An
86 example of this approach is XMapTools by Lanari et al. (2014), a graphical, open-source automated mineralogy
87 solution with multiple machine-learning classification algorithms within a standalone, MATLAB-based
88 environment.

89
90 Random forest (RF) classification is a supervised classification algorithm (i.e., the user generates training data) in
91 which an ensemble of decision trees produces a majority vote that assigns a thematic classification to unknown
92 data (Breiman, 2001). Each decision tree within the ensemble is trained on a random sample of the training data
93 using only a set number of random features at each branch (Cutler et al., 2011). During prediction, for each
94 decision tree, unknown data traverses a sequence of rule-based branches which culminate in the assignment of a

95 predicted class (Breiman, 2001). Each tree gets one vote for each pixel; the predicted class with the most votes is
96 assigned to the unknown data. There are several reasons why RF classification is useful for automated
97 mineralogy mapping. It is well suited for accommodating unbalanced training data and nonparametric data
98 distributions (Maxwell et al., 2018), which are common in rock samples due to large differences in relative
99 mineral abundances and elemental intensities (Ahrens, 1954). In addition, recent work showed that RF
100 classification performed better than other legacy machine-learning algorithms (e.g., support-vector machines;
101 Hearst et al., 1998) in mineral classification of reservoir rocks (Li et al., 2021).

102

103 The main goal of this study is to present a new, user-friendly quantitative automated mineralogy method that we
104 developed and implemented within QGIS, a free and open-source geographic information system. Unlike
105 previous methods, the method presented here uses only freely available and open-source applications, and it
106 requires no programming by the user. We use the free and open-source Orfeo Toolbox plugin for QGIS
107 (Grizonnet et al., 2017) to predict thin-section scale bulk mineralogy from EDS elemental intensity data using a
108 RF image classifier (Breiman, 2001). Situating the workflow within a GIS environment has advantages over
109 standalone programs such as direct access to raster and vector manipulation and analysis tools and database
110 management (Tarquini and Favalli, 2010; Berrezueta et al., 2019). Furthermore, we present an overview of the
111 automated mineralogy method and apply it to a set of rock samples from the Rio Blanco tonalite to demonstrate
112 the method's utility. By outlining an easy-to-use and open-source solution, we intend to provide an automated
113 mineralogy method to a broader community of users.

114

115 **2 Overview of the method**

116

117 The goal of our automated mineralogy method is to produce quantitative mineralogy maps of rock thin sections
118 solely from EDS data acquired using a SEM. Here in Section 2, we briefly summarize each step needed to reach a
119 predicted mineral map. In Section 3, we demonstrate how to use the method by applying it to a set of rock thin
120 sections, during which we elaborate on the choices users need to make and the functions they need to use during
121 each step. We also provide a detailed step-by-step guide in the supplementary information (Reed et al., 2024).

122

123 The starting point for this method is elemental rasters derived from EDS-generated scans of rock thin sections.
124 For the purposes of our method, we take these scans as already measured and in hand. Generating such scans
125 requires preparing thin sections and analyzing them with a scanning electron microscope, both of which are done

126 by established procedures (Goldstein et al., 2018). The necessary output from such scans are rasters of elemental
127 intensity (counts/eV), one for each element of interest (e.g., Ca, Na, K, etc.). After the EDS elemental intensity
128 rasters have been generated, all the remaining steps in the method are conducted in QGIS. No programming is
129 required in any step. Instead, users need only be familiar with QGIS and their samples.

130

131 The first step involves importing the raw elemental intensity rasters into QGIS with no coordinate reference
132 system (Fig. 1a). This also involves compiling a list of all the minerals that will be mapped in the thin section,
133 which can be assessed based on prior knowledge, literature, and examination of EDS spectra. Our method is not
134 viable for those thin sections from completely unknown lithologies that resist efforts to identify minerals under
135 the microscope and/or manual examination of EDS data. As we describe in Section 4, we recommend restricting
136 this to minerals with sufficiently high abundance ($>0.1\%$) to be adequately trained upon. For those workers that
137 require high accuracy in very low abundance minerals, our method is not advisable.

138

139 The second step is to smooth the raw elemental intensity rasters (Fig. 1b). This is useful because EDS-generated
140 elemental intensity rasters are subject to noise, which can arise through electron beam interactions with the
141 sample (Goldstein et al., 2018). As we describe in Section 4.3, we found that this smoothing step was best done
142 with a 7-pixel radius circular mean filter, in which each pixel is assigned the mean value of the surrounding
143 pixels in a circular window (Gonzalez and Woods, 2018). We performed this on intensity rasters from the
144 example samples we applied our method to in Section 3. For this, we used the free and open-source System for
145 Automated Geoscientific Analyses (SAGA) plugin for QGIS (Conrad et al., 2015).

146

147 The third step is to gather the smoothed elemental intensity rasters into a virtual raster, a type of container for
148 multiple rasters, with one band for each element of interest (Fig. 1c). For example, if the user chooses to import
149 elemental intensity rasters for six elements, as we did in the application of this method to our samples in Section
150 3, this will result in a virtual raster with six bands. For this, we used the Geospatial Data Abstraction Library
151 (GDAL/OGR contributors, 2022), which is a standard library in QGIS.

152

153 The fourth step is to train a RF image classification model on the virtual raster (Fig. 1d). This requires generating
154 a large number (~hundreds) of small polygons on the virtual raster. Each of these small polygons must lie within
155 a single mineral, which the user must identify and assign to the polygon. Collectively, these small polygons must
156 cover all the minerals of interest in the thin section in sufficient number to train the RF model. If the user wishes

157 to assess the accuracy of the RF-predicted mineral map to a manually mapped portion of the thin section, we
158 recommend restricting the location of these small training polygons to a relatively small portion of the thin
159 section (~10-20% by area). This will ensure that other portions of the thin section can be mapped manually to
160 compare against the RF-predicted mineral map. If the user does not wish to conduct such an accuracy assessment
161 after the RF-predicted mineral map is complete, then these small training polygons can be generated anywhere
162 across the entire thin section.

163

164 After the RF model has been trained, the fifth step is to apply the trained RF model to the entire virtual raster
165 (Fig. 1e). During this step, the RF model assigns a mineral class to every pixel in the virtual raster, which yields a
166 mineral map for the entire thin section. For these RF modeling steps, we used the free, open-source Orfeo
167 Toolbox plugin for QGIS (Grizonnet et al., 2017).

168

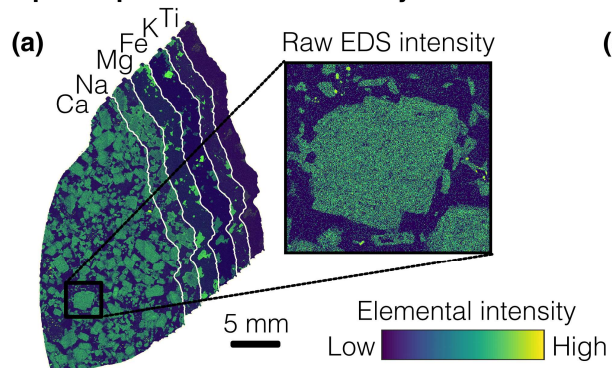
169 The sixth and final step is to denoise the RF-generated mineral map (Fig. 1f). For this, we applied a circular
170 majority filter using the SAGA plugin for QGIS, in which each pixel is assigned the modal value of the
171 surrounding pixels in a circular window (Gonzalez and Woods, 2018). As we describe in Section 4.3, we found
172 that this was best done with a 10-pixel radius majority filter in the example samples we applied this to in Section
173 3. This eliminates most isolated pixels within larger groups of pixels of a uniform predicted mineral and rare
174 pixels that were not classified due to voting ties (Ortolano et al., 2018; Nikonow et al., 2019)

175

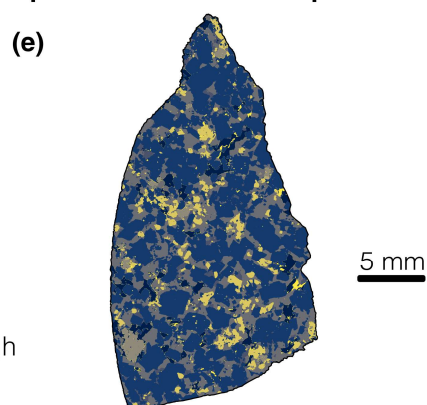
176 At this stage, the RF-predicted mineral map is complete. It can now be examined or manipulated according to the
177 user's needs. For instance, the mineral map can be converted from a raster to a vector form to facilitate
178 measurement of mineral grain size and other properties (Section 5.2).

179

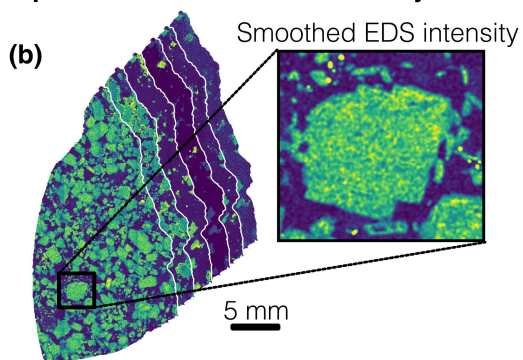
Step 1: Import elemental intensity rasters



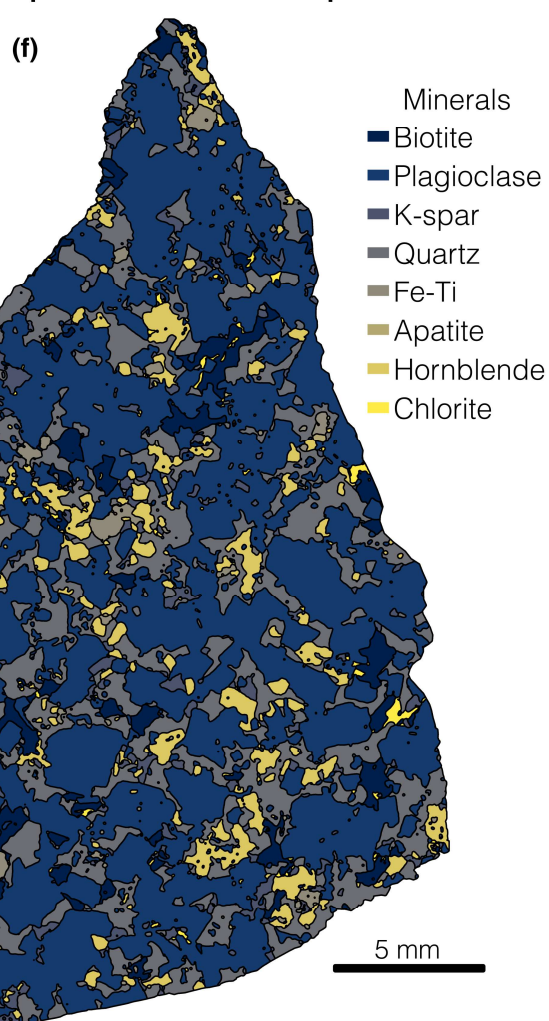
Step 5: Create mineral map



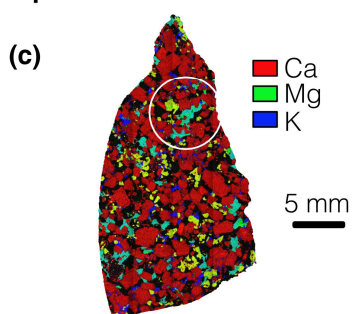
Step 2: Smooth elemental intensity rasters



Step 6: Smooth mineral map



Step 3: Create virtual raster



Step 4: Train random forest model

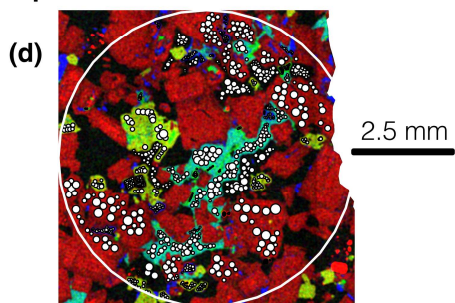


Figure 1. Example application of the automated mineralogy method. (a) Step 1: Import raw elemental intensity rasters (Ca, Na, Mg, Fe, K and Ti) into QGIS. Here, the rasters shown are for the thin-section sample 1-13a. The zoomed-in view of the Ca raster exemplifies the short-wavelength noise in the elemental rasters. (b) Step 2: Smooth each elemental intensity raster with a circular mean filter. The zoomed-in view shows that this filter has eliminated much of the short-wavelength noise that was in the raw elemental rasters. (c) Step 3: Create a virtual raster by combining the smoothed elemental rasters into a single image container with bands for each element. The white circle shows the area within which polygons were generated to train the random forest (RF) model in Step 4. (d) Step 4: Within the training area boundary in the virtual raster (large white circle, as in Step 3), draw a series of small polygons (here, small white circles). Each polygon must lie within a single known mineral, and collectively these small polygons must sample all mineral of interest (here, plagioclase feldspar, quartz, hornblende, biotite, potassium feldspar, Fe-Ti oxides, apatite, and chlorite). These polygons collect the pixel-level data on which the RF model will be trained. (e) Step 5: Apply the trained RF model to the entire sample to create a thin section-scale mineral map. (f) Step 6: Smooth the RF-predicted mineral map with a circular majority filter.

3 Application of the method

3.1 Preparation of rock thin sections from the Luquillo Critical Zone Observatory

To demonstrate the utility of the method described in Section 2, we applied it to 14 thin sections of Rio Blanco tonalite from the Luquillo Critical Zone Observatory (LCZO) in Puerto Rico, United States, a site that has been the subject of substantial research on the weathering of igneous rocks into saprolite and soil (White et al., 1998; Riebe et al., 2003; Stallard and Murphy, 2012; Brocard et al., 2023). The lithology is a phaneritic, plutonic igneous rock with some evidence of low-grade hydrothermal alteration (Speer, 1984). The Rio Blanco tonalite provides an ideal case study because mineral abundance has been characterized previously via quantitative X-ray diffraction (XRD) and point counting modal analysis (i.e., systematic manual identification and counting under microscope; Ingersoll et al., 1984), which indicated the rock consists of plagioclase feldspar (andesine), quartz, biotite, hornblende, potassium feldspar, magnetite, apatite, and chlorite (Murphy et al., 1998; Buss et al., 2008; Ferrier et al., 2010).

196 To ready the samples for EDS, 14 petrographic thin sections were prepared on 27 x 46 mm glass slides from
 197 bedrock core quarters collected from the Rio Icacos catchment within the LCZO (Comas et al., 2019). The
 198 samples ranged in area from 34.7 to 139.5 mm². Four samples are composed of weathered rock nearer to the
 199 surface while the rest are more pristine bedrock (Orlando et al., 2016). From each core depth, two thin sections
 200 were prepared in vertical and horizontal orientations. Our own preliminary optical microscopy observations
 201 revealed that these samples contained abundant plagioclase, quartz, hornblende, and biotite, which is consistent
 202 with previous modal analyses (Murphy et al., 1998; Buss et al., 2008).

203

204 **3.2 Measuring elemental intensity in thin sections with energy dispersive spectroscopy**

205 Each thin section was mapped with energy dispersive X-ray spectroscopy (EDS) using a Hitachi S-3400 VP-
 206 SEM with a thermionic tungsten electron source equipped with an Oxford Instruments X-Act 10 mm² silicon drift
 207 detector receiving X-rays across 2048 spectral bands. The EDS detector acquires a spectrum showing the energy
 208 and intensity of characteristic X-rays emitted from the sample to determine the atomic composition of the sample
 209 within the analysis volume of the primary beam (Goldstein et al., 2018). For the measurements on our thin
 210 sections, the instrument and accompanying software produced full thin-section elemental intensity maps
 211 (counts/eV) at a resolution of 4 µm/pixel, which was determined by the beam step size. EDS data were acquired
 212 with accelerating voltage of 15 kV and beam current of ~10 nA. EDS process time (also known as ‘time constant’
 213 by some manufacturers) was 4, which is an intermediate value that balances acquisition time and data quality.
 214 EDS acquisition time was ~3.5 hours for each thin section.

215

216 From the EDS analysis application included with this instrument (AZtec), we exported six TIF files for each
 217 sample (Fig. 1a) consisting of full-resolution elemental intensity rasters for the elements of interest (Ca, Na, K,
 218 Mg, Fe and Ti). These rasters contain the X-ray counts of elemental intensity at each pixel and have a mean size
 219 of over 20 megapixels over the 14 studied thin sections. We selected these elements because they are present in
 220 varying abundance in the minerals within the Rio Blanco tonalite and, hence, are useful for distinguishing among
 221 the minerals in these samples. For example, K, Mg, Fe, and Ti are present at high abundance in biotite (Dong et
 222 al., 1999) but are present at low abundance in other major minerals in this lithology (e.g., plagioclase feldspar,
 223 quartz). Our initial attempts at classification showed that the inclusion of rasters of Si and Al had no effect on
 224 classification accuracy, so we did not include them here.

225

226 This method requires a list of minerals present in the samples for both training of and prediction by the RF
227 models (Steps 4 and 5 in Section 2). Such a list can be obtained in a variety of ways, including prior studies of
228 qualitative mineralogy of the host lithology or mineral identification from optical microscopy on the sample thin
229 sections. For the 14 samples analyzed here, we generated a list of minerals by inspecting the EDS-generated X-
230 ray spectral data within Oxford AZtec, a proprietary software package integrated with the SEM that we used to
231 measure EDS scans of our samples. From these spectra we identified plagioclase feldspar, quartz, hornblende,
232 biotite, potassium feldspar, Fe-Ti oxides (predominantly magnetite-titanomagnetite), and apatite as mineral
233 classes for the RF models (Section 3.3). For those without offline access to a full EDS environment, some
234 systems such as Oxford AZtec allow for the full export of data into text or binary formats, which can be accessed
235 with free and open-source tools (e.g., HDFView or NIST DTSA-II). Due to trace abundance (Murphy et al.,
236 1998), other minerals present in the samples like epidote and titanite lacked an adequate number of trainable
237 examples, so were neglected or combined with an associated mineral, Fe-Ti, respectively. For reference, the
238 mean abundance of apatite, the lowest abundance mineral we trained, was ~0.1%. We recommend that minerals
239 present at abundances lower than this be omitted or combined with the understanding that overall accuracy is
240 most likely being negatively impacted in a minor way.

241

242 **3.3 Smoothing and virtualization of the elemental intensity rasters**

243 We smoothed each elemental intensity raster with a 7-pixel radius circular mean filter using SAGA's Simple
244 Filter tool to eliminate noise in the EDS data. We chose this filter size because it optimized the accuracy
245 calculated during the training and validation of the RF model. We test the sensitivity of this choice in Section 4.3.
246 We then used the GDAL gdalbuildvrt command within QGIS to group the smoothed elemental intensity rasters
247 into a virtual raster dataset, in which each elemental raster is represented as a separate band. A virtual raster is a
248 container for multiple rasters that encodes metadata such as file locations and other attributes in extended markup
249 language (XML) (McInerney and Kempeneers, 2014). Opening and processing virtual raster datasets requires
250 less computer resources as the underlying rasters are only accessed when required.

251

252 **3.4 Training random forest models for mineral classification**

253 Before a RF model can be tasked with assigning a mineral class to every pixel in an entire thin section, it must
254 first be trained upon the minerals in the thin section. On each of the virtual rasters for the 14 thin sections, we
255 selected an area encompassing less than ~15% of the total thin-section sample area within which we trained the
256 model. We selected training areas that represented all minerals as well as possible, so that each mineral would

257 receive an adequate amount of training data for each mineral. Selecting a small training area in the thin section is
258 useful because it enables users to test the accuracy of the trained model on other areas of the thin section, if
259 desired. This is not a necessary step in the method, but in Section 4 we show how such accuracy tests can be done
260 on other portions of the thin sections.

261

262 For each mineral within the training area, we manually generated hundreds of circular polygons upon the virtual
263 raster using the knowledge gained previously from examining the EDS spectra (Fig. 1). A single training polygon
264 within the training area collects all pixel values contained within it from each elemental intensity raster
265 composing the virtual raster. Labelling this polygon as a single mineral, effectively labels every pixel value
266 contained within it as that mineral. We note that during this training step, the user should take care not to
267 misidentify or neglect training upon abundant minerals, which could have a detrimental effect on the
268 classification accuracy. To prevent this outcome, we used all available elemental rasters to verify that training
269 polygons were within the bounds of the identified mineral. For a few thin sections, multiple subareas composed
270 the training area to incorporate enough data on less abundant minerals like apatite. Because each training polygon
271 encompassed pixel-level data for all bands from the virtual raster, the training datasets were large ($>10^5$ pixel-
272 level samples for each thin section). Hundreds to thousands of pixel-level training samples per class are generally
273 considered sufficient for RF models (Cutler et al., 2012). Training samples per mineral were highly unbalanced
274 (i.e., some minerals covered many more pixels than others) due to the high abundances of quartz and plagioclase
275 relative to those of minor mineral like apatite. Orfeo Toolbox handles this potential problem automatically by
276 randomly selecting samples at a rate relative to the size of the smallest class, ensuring that the minority classes
277 like apatite have an equal probability of being drawn into a sample subset used to construct an individual decision
278 tree.

279

280 Using the training data obtained from the virtual raster for each thin section, we trained RF image classification
281 models using the TrainImagesClassifier function in Orfeo Toolbox. In this function, users must select
282 hyperparameter values for the RF model, which are tuneable parameters that control model behaviour. In
283 machine learning, hyperparameters define the general behaviour of a model, and are distinct from model
284 parameters, which are learned through training. For more details about RF machine learning models
285 hyperparameters, see the review in Probst et al. (2019). We used the default hyperparameter values pre-selected
286 in Orfeo Toolbox (Table 1) for the models employed for our final predicted mineral maps.

287

288 A measure of model accuracy is automatically calculated by the TrainImagesClassifier function at this step using
 289 unseen training data, which can be useful to examine before proceeding as to ensure that the RF model is
 290 operating correctly. The accuracy metric we focus on in this study is the F1 score (Equation 3), which is the
 291 harmonic mean of the precision metric (Equation 1) and the recall metric (Equation 2). This is a useful measure
 292 of the accuracy of RF-predicted minerals because it penalizes false positives and false negatives while rewarding
 293 true positives and neglecting true negatives (Chinchor and Sundheim, 1993), which can be very plentiful for low
 294 abundance minerals.

$$Precision = \frac{True\ positives}{True\ positives + False\ positives} \quad (1)$$

$$Recall = \frac{True\ positives}{True\ positives + False\ negatives} \quad (2)$$

$$F1\ score = \frac{2(Precision)(Recall)}{Precision + Recall} \quad (3)$$

298
 299 In the application of Equations 1-3 to mineral maps, a true positive is defined as pixel-level agreement on the
 300 presence of a given mineral between the model prediction and unused training data, which the algorithm holds
 301 out from training for the purpose of calculating metrics such as the F1 score. Similarly, a true negative is
 302 agreement on the absence of a given mineral class. False positives and false negatives are disagreements on the
 303 presence and absence of a given mineral class, respectively. Application of the default hyperparameters to our
 304 samples yielded very high F1 scores (~0.99). This gave us confidence that the predicted mineral maps generated
 305 using the default hyperparameters were near optimal for comparison with manually delineated test maps
 306 (described in Section 4.1).

Table 1. Default hyperparameter values for Orfeo Toolbox RF machine learning model and typical values according to Probst et al. (2019).

Parameter name	Orfeo Toolbox value	Typical value(s)
Maximum number of trees in the forest	100	500-1000
Maximum depth of tree	5	N/A
Size of the randomly selected subset of features at each tree node	(number of features) ^{1/2}	(number of features) ^{1/2}

We applied each trained model to its corresponding virtual raster to predict a single mineral class at each pixel, except in the case of ensemble voting ties, in which case no mineral class was assigned to that pixel. This resulted in mineral maps at the same resolution as the virtual rasters ($\sim 4 \mu\text{m}$).

3.5 Using the random forest models to generate mineral maps

In our application of the trained RF models to our thin sections, the models calculated the entire thin-section scale mineral maps in under a minute using a desktop computer (4 GHz processor; 64 GB memory). Figure 1 shows an example of one of these mineral maps.

After a thin section's mineral map has been generated, it is trivial to calculate the abundance of each mineral by counting pixels. Figure 2 shows the abundance of each mineral across all 14 samples with the error given by the mean F1 scores of the minerals. It also reveals relatively little variation in each mineral's abundance among the 14 samples, which is consistent with previous observations of the Rio Blanco tonalite. The RF-predicted mineral abundances compare well with those measured from modal analysis via point counting on BSE imagery (Buss et al., 2008) and via quantitative XRD (Ferrier et al., 2010). Buss et al. (2008) measured average areal abundances of 19.9% and 49.3% for quartz and plagioclase, respectively, comparable to the RF-predicted average abundances of $22.8 \pm 1.0\%$ and $55.8 \pm 2.3\%$ (\pm error from mean F1 scores) on our 14 thin sections. The combined abundance of hornblende and biotite ('Fe-silicates') measured by Buss et al. (2008) was 24%, which is close to the maximum RF-predicted abundance of 'Fe-silicates' among our 14 samples ($25.0 \pm 1.5\%$). Using common values for molar masses (M mol^{-1}) and densities (M L^{-3}), the XRD-based abundances (converted to areal abundance) from Ferrier et al. (2010) for quartz, plagioclase, and hornblende were 24%, 62%, and 14%, respectively, while the RF-predicted mineral maps yielded $22.8 \pm 1.0\%$, $55.8 \pm 2.3\%$, and $10.4 \pm 0.7\%$, respectively. When quartz, plagioclase, and alkali feldspar abundances are normalized for usage with a Quartz-Alkali Feldspar-Plagioclase-Feldspathoid diagram (Le Maitre, 2002), the RF-predicted abundances for each mineral demonstrated that all thin sections can be classified as tonalite, matching the name of the lithology.

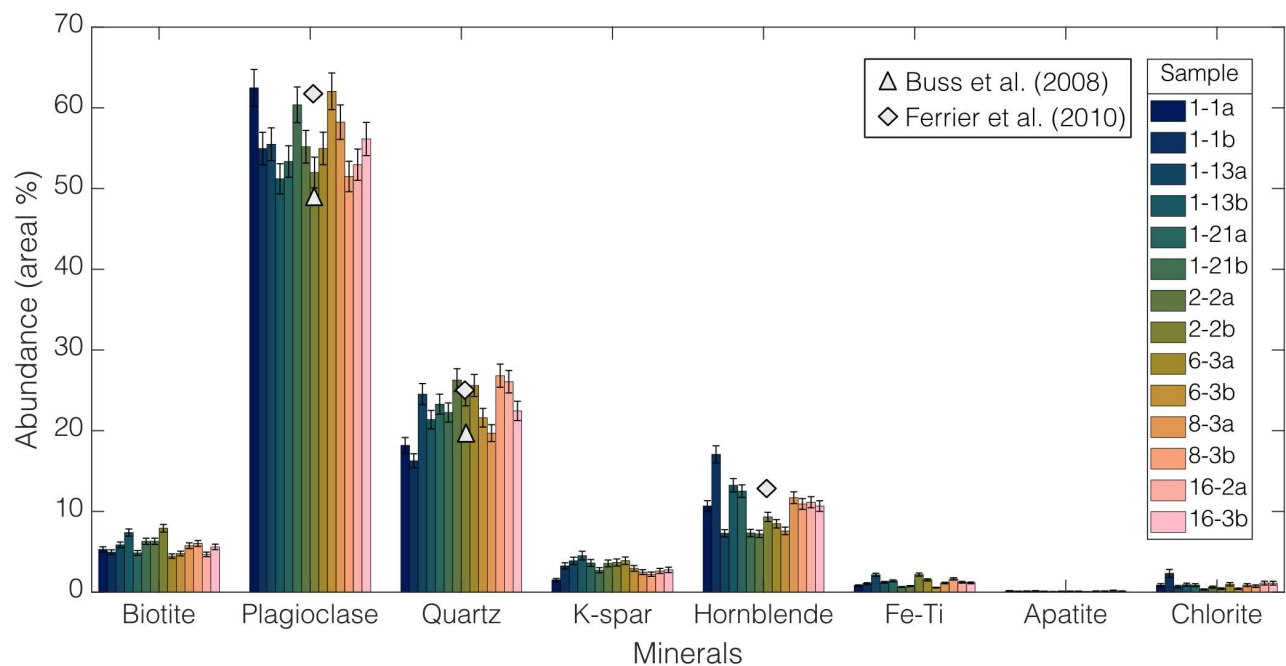


Figure 2. Areal abundance for all 14 samples of the Rio Blanco tonalite. Error bars stem from mean F1 scores for each individual minerals from test map comparisons (see Section 4.1). Data from the analyses of the Rio Blanco tonalite in Buss et al. (2008) and Ferrier et al. (2010) included for reference.

4. Discussion: Accuracy of random forest-predicted mineral maps and sensitivity analyses

4.1 Accuracy of random forest-predicted mineral maps

Before applying the trained RF models to the full thin sections, we manually mapped the mineralogy of a small section for three representative samples (6-3a, 16-2a, and 1-13a) to assess the accuracy of the model-generated mineral maps. We refer to these manually delineated mineral maps as “test maps”. These test maps were manually delineated as vector polygons for all mineral classes using the elemental intensity rasters for guidance. For example, when mapping a grain of potassium feldspar, we determined the boundaries of the grain with filtered and unfiltered rasters of K as well as combined intensity rasters of multiple elements. We consider these maps to be ‘ground truth’ data, which are never perfect representations of reality (Foody, 2024), but, nonetheless, may serve to compare the performance of this method to the extremely slow process of manually mapping grain boundaries. We then rasterized the manually-delineated vector maps, which resulted in the classification of every pixel within the test maps as one of the eight minerals. The test maps averaged over 1 million pixels in size.

351

352 We compared the same section of the predicted mineral maps to the test maps using a frequency-weighted F1
353 score (Equation 4) to gauge the average accuracy for all mineral classes. To calculate a frequency-weighted F1
354 score, the F1 score for the i^{th} class ($F1\ score_i$) is weighted by the class frequency (w_i), which is the proportion of
355 pixels of class i to the total number of pixels in the test map. Here, N is the number of mineral classes.

356

$$Frequency - weighted\ F1\ score = \sum_{i=1}^N w_i F1\ score_i \quad (4)$$

357

358 We clipped the portion of the predicted mineral map overlapping the test map from the full map for each of the
359 three thin sections with a test map. From these two rasters, we calculated the frequency-weighted F1 score.

360

361 The RF-generated mineral maps in Section 3 exhibited high accuracy. For the three thin sections that were
362 mapped both manually and by the RF-based method in Section 2, the mean frequency-weighted F1 score among
363 the three thin sections was 0.948 ± 0.002 , meaning that nearly 95% of the pixels in the RF-predicted maps agreed
364 with those in the manually delineated maps (Table 2). The accuracy varied among minerals. The four most
365 abundant minerals (plagioclase, quartz, hornblende, and biotite) all have mean F1 scores of 0.94 to 0.96, while
366 apatite, the least abundant mineral, had the lowest mean F1 score of 0.72. A closer look at the precision and recall
367 metrics for apatite show that mean recall scores (0.62) were lower than mean precision (0.91). This indicates that
368 the models correctly predicted apatite when attempted but the models often neglected to predict apatite. Because
369 apatite is rare and appears as small inclusions in our samples, less training data was collected for it than for other
370 minerals in each sample. This can result in class imbalances in training data, which, for rare mineral classes (in
371 our case, apatite), can produce scenarios in which the model does not try to predict the mineral class, as the
372 diversity of training data for rare classes (in our case, apatite) remains relatively low (He and Garcia, 2009).
373 Abundance and the mean F1 score were not always linked; for example, Fe-Ti oxides were low in abundance
374 ($\sim 1\%$) but registered a mean F1 score of 0.91.

375

376 Figure 3 shows an example of an RF-predicted mineral map with misclassified pixels shown in red. This
377 illustrates a key point: the accuracy of the RF-predicted mineral maps is not spatially uniform. Most pixels that
378 diverge from manual classification occur at grain boundaries where elemental compositions shift abruptly in

379 space. By contrast, in mineral grain interiors, divergent pixels are far less common. This indicates that the
380 accuracy of RF-predicted mineralogy in grain interiors is higher than the F1 scores in Table 2.

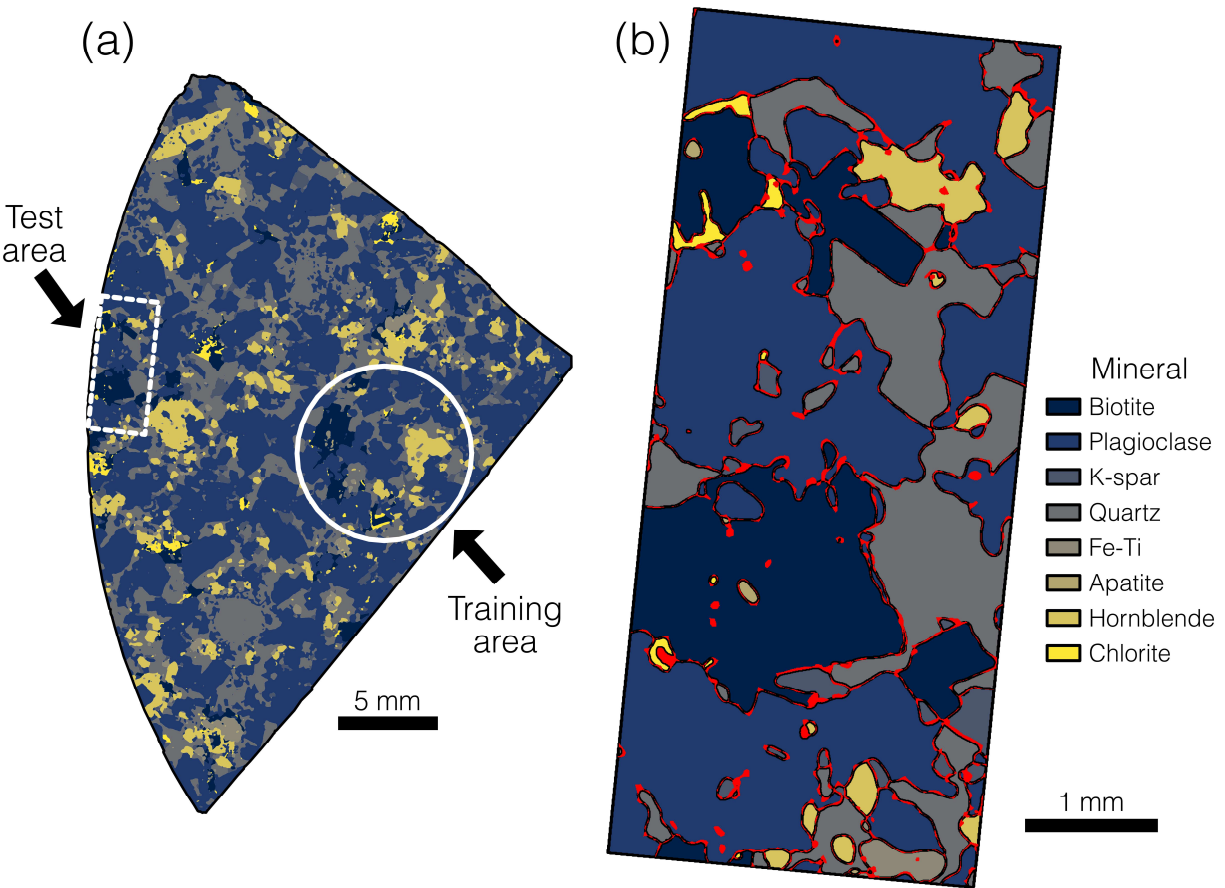


Figure 3. (a) Predicted mineral map for sample 6-3a, showing the location of the manually delineated test map, which we used to check accuracy. (b) Predicted mineral map for the test area. Red color signifies where pixels in the predicted map diverge from the manually delineated test map. This shows that most divergent pixels are at mineral grain boundaries.

381
382 A combined confusion matrix for pixel-level comparisons from every test and predicted map showed the most
383 common divergent classification was chlorite for biotite. This is likely because biotite and chlorite have similar
384 elemental compositions and because they often share a grain boundary (chlorite is a product of hydrothermal
385 alteration of biotite), which means they are more prone to disagreement along grain boundaries. Among the major

minerals, our models divergently classified potassium feldspar as plagioclase feldspar most often, likely because many potassium feldspar grains in the Rio Blanco tonalite contain small amounts of Na, like plagioclase.

Figure 4 shows close agreement between the RF-predicted abundance and the manually mapped abundance in the test areas, with a mean difference for a given mineral of $0.45 \pm 0.02\%$ across the three test maps. So, although some predicted pixels were misaligned spatially, the RF-predicted mineral abundances agree well with manual estimates derived from the test maps.

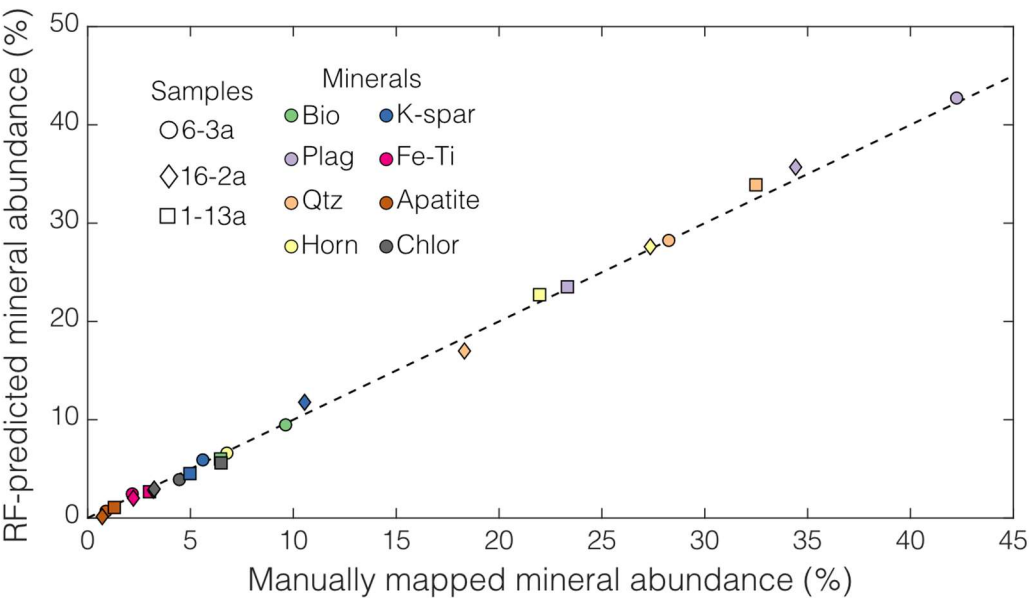


Figure 4. RF model-predicted mineral abundance vs. manually mapped mineral abundance in the test areas of the three samples with test maps. The dashed line is a 1:1 line. Although there was some spatial mismatch around the edge of mineral grains (e.g., Fig. 3), the RF-predicted modal abundances agree well with abundances inferred from manual mapping in the test areas.

393
394

Table 2. Mean F1 scores (accuracy metric) for mineral classes among the three test maps (Fig. 4), based on comparison of automated mineralogy maps to manually delineated mineralogy maps.

Mineral	Mean F1 score
---------	---------------

All classes (frequency-weighted)	0.95
Plagioclase feldspar	0.96
Quartz	0.94
Hornblende	0.94
Biotite	0.94
Potassium feldspar	0.88
Fe-Ti oxides	0.91
Chlorite	0.79
Apatite	0.72

4.2 Sensitivity of mineral maps to random forest hyperparameters and input features

In our application of the method in Section 2 to the 14 samples in Section 3, we used a set of default values for three RF hyperparameters: maximum tree depth, number of trees, and minimum sample size per node. Reviews of hyperparameter tuning on RF models have shown that the number of trees and the minimum number of classes per node can have a large effect on classification accuracy (Probst et al., 2019). In this section we gauge the sensitivity of our results to hyperparameter values and input features.

Orfeo Toolbox does not contain a facility for hyperparameter tuning in QGIS, so we developed a workflow to undertake our own hyperparameter optimization outside of QGIS in Python. This is not a necessary step in the method, but we have included this code in the Supplement for users who wish to conduct their own hyperparameter optimization. We began by converting the smoothed elemental intensity image data in the three training areas within the manually delineated test maps into NumPy arrays (Harris et al., 2020) using a combination of three Python libraries: rasterio (Gillies et al., 2019), geopandas (Jordahl et al., 2020), and shapely (Gillies et al., 2022). We then used the implementation of the RF classifier from the machine-learning package scikit-learn (Pedregosa et al., 2011) for both hyperparameter optimization using a randomized five-fold cross validation (Breiman and Spector, 1992) and derivation of feature importance using permutation testing (Breiman, 2001). Through these operations we seek to find optimal hyperparameters and test the importance of input features (here, elements), respectively.

We used the scikit-learn RandomizedGridCV function to systematically test the sensitivity of the output mineral maps to the RF hyperparameter values. To do this, we trained 100 unique RF models across a range of maximum

tree depth (1-100), number of trees (10-2000), and minimum sample size per node (5-25). These hyperparameters are common between the Orfeo Toolbox and scikit-learn implementations of the RF classifier. We used five-fold cross-validation, in which each randomly selected set of hyperparameters is used to train the same model five times while sampling different portions of the training data (Breiman and Spector, 1992). We report the best fit parameters and resultant accuracy in terms of the frequency-weighted F1 score upon comparison to the test maps using these optimized parameters.

Orfeo Toolbox has not yet incorporated a capacity to derive feature importance scores. Feature importance in RF classification is calculated by permutation testing, which is the extent to which an accuracy metric declines if a single input feature's unused training data is randomly altered during the training process and validation process (Breiman, 2001; Guo et al., 2011). We used the sci-kit learn function `permutation_importance` to assess importance using the frequency-weighted F1 score. We report the feature importance for the three samples with manually delineated test maps and discuss their implications.

Tuning the hyperparameters in scikit-learn showed that both a higher maximum tree depth and number of trees may be optimal for our RF models, while the minimum sample for splitting was more variable (Table 3). Using these optimized RF hyperparameters within Orfeo Toolbox yielded a mean frequency-weighted F1 score of 0.95 when comparing the three samples with manually delineated test maps, which is the same F1 score realized by using the default hyperparameters. As the two implementations of the RF classifier are somewhat different in terms of available hyperparameters, the comparison is imperfect but does provide a check to see if the default hyperparameters could be improved upon. That an optimized set of hyperparameters delivered very little to no increase in accuracy is unsurprising as RF models are known to perform well with little to no tuning if reasonable hyperparameter values are initially used (Maxwell et al., 2018). Unless low F1 scores are realized during Step 4, it is our recommendation that the default RF hyperparameters in Orfeo Toolbox be used.

Table 3. Optimal RF hyperparameters from five-fold cross validation performed using sci-kit learn.

Sample	Maximum tree depth	Number of trees	Minimum sample for split
--------	-----------------------	--------------------	-----------------------------

1-13a	73	1685	25
6-3a	94	1371	5
16-2a	73	1581	5

443

444

445 Feature importance, as determined through permutation testing, showed that both K and Mg were the most
446 important features for our scikit-learn trained models with mean decreases in accuracy based on frequency-
447 weighted F1 scores derived from the training and validation process on unused data of 0.29 for both elements
448 (Fig. 5). Ti was relatively unimportant with a very small, slightly positive value, implying it could be omitted.
449 Although Ti is present within biotite and Fe-Ti oxides in our samples, Ti showed little to no decrease in mean
450 accuracy as both biotite and Fe-Ti oxides can be classified using other elements. We tested whether our feature
451 importance scores were pertinent to models in Orfeo Toolbox by leaving out, in turn, K, Mg, and Ti during
452 training and validation process. Excluding K decreased mean F1 scores due to the degradation of potassium
453 feldspar, biotite, and chlorite accuracy. In contrast, omitting Mg did not decrease F1 scores, showing that a
454 feature importance score does not directly translate to decreased model accuracy upon omission (Cutler et al.,
455 2011). Leaving out Ti had little effect on F1 scores. If a user of our method is unsure whether an element could
456 be a truly important feature, omitting an important element from the training process by creating virtual rasters
457 without that element should yield a notable degradation in training F1 scores.

458

459

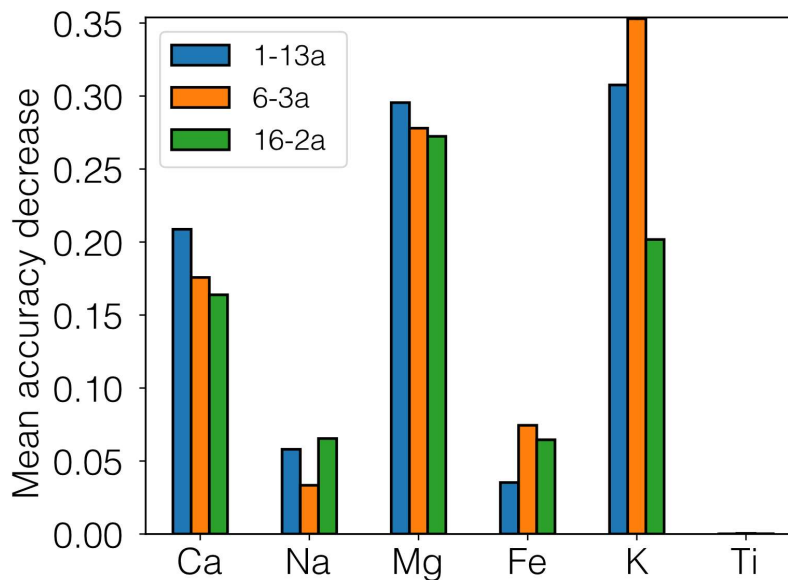


Figure 5. Feature importance from scikit-learn using permutation testing for all six input elements for the three samples with test maps. Mean accuracy decrease is the change in the F1 score due to randomly changing feature data in the unused portion of the training data during the validation process. In Orfeo Toolbox, training models that omitted K degraded F1 scores while those that omitted Mg yielded little change, indicating that feature importance score does not always directly map onto model accuracy and that some experimentation with input features (elements) during the training phase is warranted.

460

461 **4.3 Sensitivity of mineral maps to filter sizes**

462 In our application of this method to our samples, we applied a circular, 7-pixel radius mean filter to the EDS-
 463 generated elemental intensity rasters (Step 2 in Section 2), and we applied a circular, 10-pixel radius majority
 464 filter to the output mineral maps (Step 6). To quantify the sensitivity of the output mineral maps to these “hidden”
 465 parameters, we generated a series of RF models across a range of mean filter radii for the elemental intensity
 466 rasters (no filter, 2, 5, 7, 10, and 20 pixels) and a range of majority filter radii (no filter, 2, 5, 7, 10, and 20 pixels).
 467 For the three thin sections with manually delineated mineral maps, we calculated the frequency-weighted F1
 468 score of the entire thin section by comparing each of the RF-predicted mineral maps to the manually delineated
 469 test maps.

470

471 Figure 6 reveals that both the mean filter and the majority filter affect the accuracy of the predicted mineral maps.
472 The largest impact on the accuracy, as measured by F1 score, was in the application of any mean filter at all to
473 the input elemental intensity rasters. The left panel in Fig. 6 shows that applying no mean filter to the elemental
474 intensity rasters produced low F1 scores (0.52-0.69) for all models and all samples, regardless of the size of the
475 majority filter. Accuracy increased with mean filter radius up to 5 and 7 pixels, which yielded high F1 scores at
476 all majority filter sizes (0.91-0.96) due to the elimination of spurious inclusions within larger mineral grains
477 (middle panels in Fig. 6). Beyond that size, accuracy decreased slightly with higher mean filter radius, with lower
478 F1 scores at radii of 10 pixels (F1 scores of 0.90-0.95) and 20 pixels (0.87-0.89). This implies an intermediate
479 optimal mean filter radius of 5-7 pixels for these samples.

480

481 Accuracy was sensitive to the size of the majority filter, particularly for models that applied no mean filter or a
482 small (2-pixel radius) mean filter to the input elemental intensity rasters (Fig. 6). For the models that applied a
483 mean filter of any size, accuracy was lower at small majority filter radii (0 or 2 pixels) and large radii (20 pixels)
484 than at intermediate majority filter radii (5-10 pixels). At the largest radii, the RF-predicted mineral grains begin
485 to lose shape, becoming more circular. Thus, accuracy was maximized at intermediate majority filter radii of 5-7
486 pixels, just as it was at intermediate mean filter radii. Excluding plagioclase and quartz (which generally do not
487 occur as isolated grains), the three samples with test maps (6-3a, 1-13a, and 16-2a) have a median grain area of
488 $\sim 0.005 \text{ mm}^2$ ($n = 5188$ mineral grains across all three samples) while the 5-7-pixel radii filters have areas of
489 $\sim 0.001 \text{ mm}^2$ and $\sim 0.002 \text{ mm}^2$, respectively. These optimal sizes most likely result from a mix of the initial EDS
490 pixel resolution and data quality and the types and sizes of minerals in the thin section (Lanari et al., 2014;
491 Ortolano et al., 2018), so we recommend that users experiment to find the optimum filter sizes for their samples.

492

493

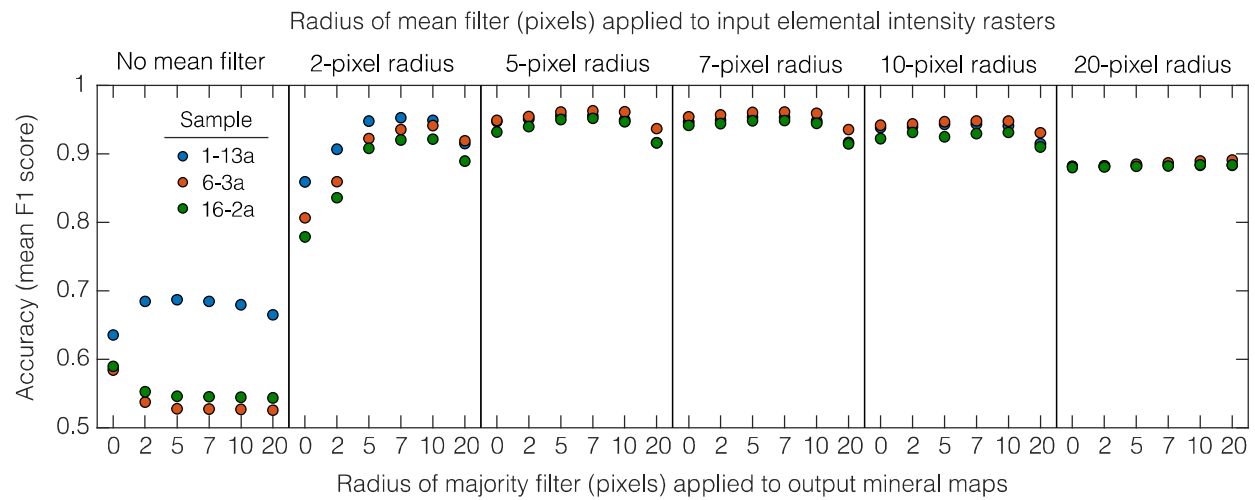


Figure 6. Accuracy of the output mineral maps (as quantified by frequency-weighted mean F1 scores) for combinations of mean filter and majority filter sizes for the three samples with test maps. Each section is a single mean filter size. The most accurate mineral maps (i.e., those with the highest F1 scores) were generated using a 5- or 7-pixel radius mean filter combined with a 5- or 7-pixel radius majority filter.

5 Discussion: Advantages, utility, and limitations

5.1 Advantages of this open-source automated mineralogy method

Situating our workflow in a free and open-source GIS environment confers several practical benefits. Both Orfeo Toolbox and QGIS are frequently updated with source code that can be examined and modified, unlike many proprietary hardware/software systems (Keulen et al., 2020). Orfeo Toolbox and QGIS each have extensive documentation and user forums monitored by the developers, which can aid in addressing user issues (Raza and Capretz, 2015). Incorporating open-source software into scientific methods fosters transparency and reproducibility as the software is widely accessible and more easily scrutinized (Ramachandran et al., 2021). As both Orfeo Toolbox and QGIS are ongoing efforts with active contributing communities, our no-code workflow is tied to software that is not likely to fall into disrepair or unavailability, unlike much open-source scientific software (Coelho et al., 2020). Furthermore, both Orfeo Toolbox and QGIS are available for all major operating systems, Windows, macOS (Intel), and Linux, so this factor does not limit accessibility. Orfeo Toolbox will likely continue to incorporate new state-of-the-art machine-learning algorithms. For example, Orfeo Toolbox has

recently been unofficially extended to utilize the Google TensorFlow library (Abadi et al., 2016) to perform deep-learning tasks on remote sensing imagery (Cresson, 2018, 2022). There are also efforts to develop open-source scanning electron microscope systems and attendant software such as the NanoMi project (Malac et al., 2022). All of this means that automated mineralogy methods are likely to become more popular and accessible.

We expect that a broad range of geoscientists will be capable of using this GIS-based method, since many geoscience undergraduate programs incorporate GIS into courses (Marra et al., 2017). It requires no programming skill to obtain mineral maps, thereby eliminating a potential barrier for use (Bowlick et al., 2016). Since the workflow takes place within a GIS environment, the input elemental intensity rasters could easily be processed in other ways besides the mean smoothing filter that we applied here, such as edge-detection filtering or elemental intensity ratioing. Creation of optimal input features, so-called feature engineering, is fostered by the many QGIS frontends that interface with SAGA GIS and GDAL raster manipulation programs. Our method does not require a corresponding plugin for Orfeo Toolbox/QGIS, but much of it could be automated from the Orfeo Toolbox/QGIS Python API or as QGIS console commands, if desired. Input parameters for image filters and hyperparameters for the RF models can be saved as JavaScript Object Notation (JSON) files, which can be loaded in later, overcoming some of the reproducibility issues inherent in workflows using graphical user interfaces (Brundson, 2016).

5.2 Illustration of the utility of random forest-generated mineral maps

There are many potential uses for thin section-scale mineral maps once they have been generated. Converting the mineral maps into vector form allows for the calculation of derived parameters such as median grain area for minerals that occur as single grains (e.g., biotite), distance between grains of a mineral, and the types of minerals surrounding a grain or grains in the case of abundant, connected minerals like plagioclase and quartz. This type of data is normally generated by proprietary automated mineralogy systems but could aid in geoscience disciplines beyond ore geology or petroleum geology (Han et al., 2022). An illustrative example is in the analysis of grain-scale properties of biotite. This is of wide interest because oxidation of ferrous Fe in biotite drives expansion of biotite grains, which generates stresses in the surrounding rock that may be large enough to fracture the rock (Fletcher et al., 2006; Goodfellow et al., 2016; Goodfellow and Hilley, 2022). To the extent that biotite expansion promotes generation of regolith from bedrock, it may even influence the km-scale evolution of mountainous topography (Wahrhaftig, 1965; Xu et al., 2022). In granitic rocks, numerical modelling has shown that biotite abundance influences the accrual of microscale damage (Shen et al., 2019) and weathering profile development is

540 partially guided by biotite crystal size (Goodfellow and Hilley, 2022). These are two properties that can be
541 directly measured in our thin section-scale mineral maps.

542

543 To obtain such mineral maps in some previous studies, researchers have often engaged in manual or semi-
544 automated characterizations of sample mineral properties (Buss et al., 2008; Ündül, 2016). These workflows are
545 often tailored for a single study (e.g., Goodfellow et al., 2016). Methods that are based on generalizable
546 workflows involving automated mineralogy methods such as the one presented in this study could enhance
547 comparability between studies. Since we converted the predicted mineral maps into a vector (polygon) form
548 within QGIS, we could use built-in functions to gather large amounts of data on grain neighbours or perform
549 grain size measurements. As we discuss in Section 5.3, classified biotite ‘grains’ may contain multiple bordering
550 crystals of the same mineral as our EDS input data, and the resultant classification cannot differentiate boundaries
551 by elements alone (Lanari et al., 2014). As biotites are relatively isolated from each other in our thin sections,
552 these measurements serve as a reasonable indicator of true biotite properties. For example, the 20 largest biotite
553 grains in samples 1-1a and 6-3b comprise 80% and 94% of the total biotite area, respectively (Fig. 7a-b). The
554 median grain area of these 20 biotite grains in sample 1-1a is 0.60 mm^2 , several times larger than that in sample
555 6-3b (0.19 mm^2 ; Fig. 7c).

556

557 We can also use raster morphology operations on the mineral maps to measure distances between classified
558 minerals. In analog and numerical experiments that impose stress on granitic rocks (Tapponier and Brace, 1976;
559 Li et al., 2003; Mahboudi et al., 2012), biotite grains can act as preferential origination points for microfractures,
560 but biotite can also arrest propagation of microfractures arising from neighboring grains. Thus, the distance
561 between biotite grains may be an important, yet rarely measured property. In the example of the two samples in
562 Fig. 7, biotite grains have similar median distances from one another but different probability distributions of
563 distances between biotite grains, particularly in the long tail of the distributions at larger distances (Fig. 7e). We
564 can also extract the composition of neighbouring grains surrounding biotite (Fig. 7f), which reveal that chlorite is
565 much more abundant near biotite relative to the rest of the thin section. Data like these can be useful for those
566 studying the impacts of different grain-grain contacts on stress response during rock mechanics experiments (e.g.,
567 Aligholi et al., 2019), which has shown that some mineral interactions can have an outsized influence on the
568 development of fractures and failure. In sum, the data in Fig. 7 illustrate the potential power of RF-generated
569 mineral maps to improve quantitative in-situ investigations of biotite weathering (Behrens et al., 2021) and form
570 the basis for more realistic models of biotite-driven rock damage (Shen et al., 2019).

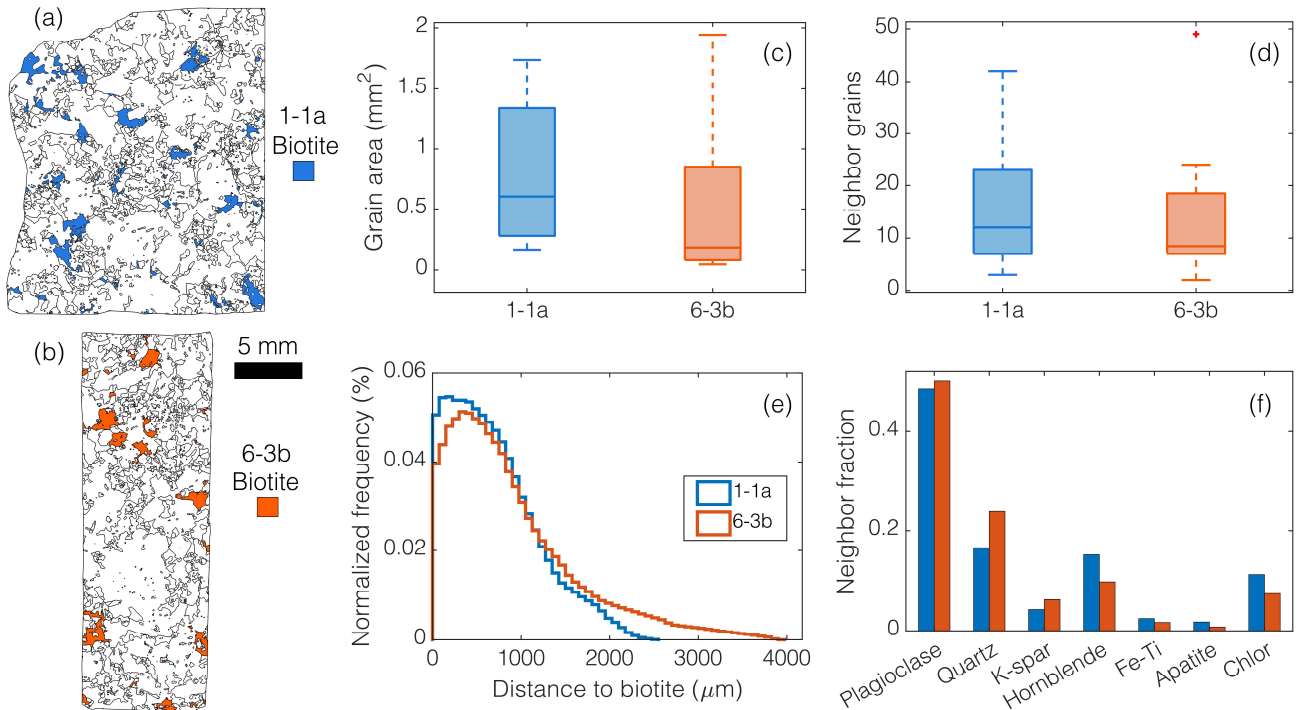


Figure 7. Example of quantities that can be obtained from mineral maps generated by the automated method in this study. (a-b). Colours highlight biotite grains identified in the RF-generated mineral maps in thin sections 1-1a (blue) and 6-3b (orange). (c-f). Biotite properties extracted from predicted maps for the 20 largest biotite grains in each sample. These data could help inform numerical models of microcrack generation and allow for quantitative comparisons between different samples or lithologies (e.g., Shen et al., 2019). (c) Boxplot of biotite grain area (mm²) for the 20 largest biotite grains for both samples. (d) Boxplot of number of grains surrounding the largest 20 biotite grains. (e) Normalized frequency distribution of distances between biotite pixels (not including those inside a biotite grain). (f) Composition of neighbours as a fraction of perimeter.

572

573

574 5.3 Limitations

575 Our method's greatest asset is that it can generate thin section-scale mineral maps without requiring the use of
 576 propriety software or a background in programming. Its most important limitation is that it is most accurate if the
 577 user trains a RF model for every thin section sample. Using a RF model that was trained on one sample to predict
 578 mineral maps for another sample can yield mineral maps that accurately map minerals in some areas but

579 inaccurately in others. For example, when we applied a RF model that was trained on sample 16-2a to sample 6-
580 3a, apatite abundance was overpredicted by a factor of 5 possibly due to 6-3a having some highly calcic zones
581 within plagioclase grains. So, for the most accurate results, we recommend training each thin section separately.

582

583 A second limitation is that this method tends to be less accurate at identifying low abundance minerals. Unlike
584 some proprietary automated mineralogy software systems, our method does not use predefined EDS spectra to
585 identify minerals. Instead, our method trains RF models on the samples themselves, which means that each
586 mineral of interest must be abundant enough to properly train the RF model. The relatively low F1 scores of the
587 lower abundance minerals in our samples (Table 2) suggest that the minimum abundance required to train a RF
588 model is larger for minerals with small grain size (e.g., in the case of apatite) and a lack of compositional
589 distinction (e.g., in the case of chlorite). Minerals must be resolvable by the EDS data, so collecting EDS data
590 with a field-emission-gun SEM at higher resolution ($\sim 0.1 \mu\text{m}$) could improve mineral classification in rocks with
591 finer grain size distributions (Han et al., 2022).

592

593 A final limitation is that mineral grains that border mineral grains of the same mineral appear to the RF model as
594 regions of the same mineral and, hence, can be classified as a single mineral grain, rather than two grains. This is
595 a common issue shared with other automated mineralogy methods (Lanari et al., 2014; Hrtska et al., 2019), and it
596 can affect inferred probability distributions of mineral grain size of those mineral if not properly accounted for.

597

598 **6. Conclusions**

599 The main contribution of this study is a new automated method for obtaining mineral maps from EDS scans of
600 rock thin sections. This method is implemented within a free and open-source GIS application, uses free and
601 open-source plugins for RF image classification, and requires no programming. To demonstrate the utility of this
602 method, we trained RF models on EDS scans of 14 thin-section samples of a well-studied, plutonic igneous rock.
603 The resulting model-predicted mineral maps compare well with manually delineated mineralogy maps, with 95%
604 of pixels on the mineral maps predicted correctly. With regards to the most abundant minerals in the Rio Blanco
605 tonalite, plagioclase feldspar and quartz, the models attained 96% and 94% accuracy, respectively.

606

607 We utilized scikit-learn's implementation of the RF classifier to search for optimal RF hyperparameters and to
608 test input feature (element) importance. We saw no increase in accuracy using optimal hyperparameters found in
609 scikit-learn when used within Orfeo Toolbox, so we recommend using the default hyperparameters. We did see

610 that an important input feature, K, did lower accuracy when not included in Orfeo Toolbox-based models, so
611 some level of experimentation with input features during the training step is warranted. We also tested to see if
612 our pre- and post-processing steps had a large influence on accuracy by using different sizes of mean and
613 majority filters. An absence of filtering and excessively large filters led to lower accuracy while filters in the
614 range of 5-10 pixels for both mean and majority filters led to higher accuracy.

615

616 Situating the workflow within a free and open-source GIS environment confers distinct advantages. Open source
617 extends benefits such as source code availability, extensive documentation, and accessibility. Moreover, as the
618 workflow is within a GIS environment, the application is likely to be familiar to a range of geoscientists. Also, all
619 the available tools (e.g., different types of image filters) within the GIS allow for easy input feature
620 experimentation. The mineral maps from our method proved highly accurate when compared to manually-
621 delineated maps, and estimates of mineral abundance compared well to previous estimates from the literature for
622 our sample lithology. Many of the measured quantities produced by proprietary automated mineralogy systems
623 are obtainable once predicted mineral maps are converted to vector datasets. These measurements, such as
624 median grain size and amount of grain neighbours, can be useful to researchers studying microscale damage
625 processes that arise through rock weathering or rock mechanics experiments. We hope that this method will be
626 useful for researchers who wish to obtain rapid, automated mineralogy maps of thin sections.

627

628 **Code and Data availability**

629 The manuscript supplement containing the code for analysis and visualizations is available through a Zenodo
630 repository (<https://zenodo.org/doi/10.5281/zenodo.10912627>; Reed et al., 2024). The supplement also contains
631 data (smoothed elemental intensity rasters, training polygons, and test maps) for the three thin sections with
632 manually delineated test maps.

633

634 **Author contribution**

635 **Miles Reed**: conceptualization, formal analysis, methodology, software, visualization, and writing (original draft
636 and preparation); **Ken Ferrier**: funding acquisition, supervision, visualization, and writing (review and editing);
637 **William Nachlas**: resources and writing (review and editing); **Bil Schneider**: investigation and writing (review
638 and editing); **Chloe Arson**: funding acquisition and writing (review and editing); **Tingting Xu**: writing (review
639 and editing); **Xianda Shen**: writing (review and editing); **Nicole West**: funding acquisition and writing (review
640 and editing).

641

642 **Competing interests**

643 The authors declare no competing interests.

644

645 **Acknowledgements**

646 This work was supported by NSF award EAR-1934458 and NSF award EAR-1755321.

647

648 **References**

- 649 Abadi, M., Agarwal, A., Barham, P., Brevdo, E., Chen, Z., Citro, C., ... and Zheng, X: Tensorflow: Large-scale
650 machine learning on heterogeneous distributed systems. arXiv [preprint],
651 <https://doi.org/10.48550/arXiv.1603.04467>, 16 March 2016.
- 652 Aligholi, S., Lashkaripour, G. R., and Ghafoori, M: Estimating engineering properties of igneous rocks using
653 semi-automatic petrographic analysis. Bull. Eng. Geol. Environ., 78, 2299-2314. [https://doi.org/10.1007/s10064-](https://doi.org/10.1007/s10064-018-1305-7)
654 [018-1305-7](https://doi.org/10.1007/s10064-018-1305-7), 2019.
- 655 Behrens, R., Wirth, R., and von Blanckenburg, F: Rate limitations of nano-scale weathering front advance in the
656 slow-eroding Sri Lankan Highlands, Geochim. Cosmochim. Acta, 311, 174-197,
657 <https://doi.org/10.1016/j.gca.2021.06.003>, 2021.
- 658 Berrezueta, E., Domínguez-Cuesta, M. J., and Rodríguez-Rey, Á: Semi-automated procedure of digitalization and
659 study of rock thin section porosity applying optical image analysis tools, Comput. Geosci., 124, 14-26,
660 <https://doi.org/10.1016/j.cageo.2018.12.009>, 2019.
- 661 Bjørlykke, K: Relationships between depositional environments, burial history and rock properties. Some princi-
662 pal aspects of diagenetic process in sedimentary basins, Sediment. Geol., 301, 1-14,
663 <https://doi.org/10.1016/j.sedgeo.2013.12.002>, 2014.
- 664 Blannin, R., Frenzel, M., Tuşa, L., Birtel, S., Ivăşcanu, P., Baker, T., and Gutzmer, J: Uncertainties in quantitative
665 mineralogical studies using scanning electron microscope-based image analysis, Miner. Eng., 167, 106836,
666 <https://doi.org/10.1016/j.mineng.2021.106836>, 2021.
- 667 Breiman, L: Random forests, Mach. Learn., 45, 5-32, <https://doi.org/10.1023/A:1010933404324>, 2001.
- 668 Breiman, L., and Spector, P: Submodel selection and evaluation in regression: The X-random case, Int. Stat.
669 Rev., 291-319, <https://doi.org/10.2307/1403680>, 1992.
- 670 Brocard, G., Willebring, J. K., and Scatena, F. N: Shaping of topography by topographically-controlled vegetation
671 in tropical montane rainforest, PLoS One, 18(3), e0281835, <https://doi.org/10.1371/journal.pone.0281835>, 2023.
- 672 Brunson, C: Quantitative methods I: Reproducible research and quantitative geography, Prog. Hum. Geogr.,
673 40(5), 687-696, <https://doi.org/10.1177/0309132515599625>, 2016.

674 Bürgmann, R., and Dresen, G: Rheology of the lower crust and upper mantle: Evidence from rock mechanics,
675 geodesy, and field observations, *Annu. Rev. Earth Planet. Sci.*, 36, 531-567, <https://doi.org/10.1146/annurev.earth.36.031207.124326>, 2008.

677 Buss, H. L., Sak, P. B., Webb, S. M., and Brantley, S. L.: Weathering of the Rio Blanco quartz diorite, Luquillo
678 Mountains, Puerto Rico: Coupling oxidation, dissolution, and fracturing, *Geochim. Cosmochim. Acta*, 72(18),
679 4488-4507, <https://doi.org/10.1016/j.gca.2008.06.020>, 2008.

680 Callahan, R. P., Riebe, C. S., Sklar, L. S., Pasquet, S., Ferrier, K. L., Hahm, W. J., ... and Holbrook, W. S.: Forest
681 vulnerability to drought controlled by bedrock composition, *Nat. Geosci.*, 15(9), 714-719,
682 <https://doi.org/10.1038/s41561-022-01012-2>, 2022.

683 Callister, W. D., and Rethwisch, D. G.: Callister's Materials Science and Engineering, Global Edition, 10th Edi-
684 tion, John Wiley & Sons, ISBN 978-1-119-45520-2, 2019.

685 Chinchor, N., and Sundheim, B. M: MUC-5 evaluation metrics, in: Proceedings of the Fifth Message Understand-
686 ing Conference (MUC-5), August 25-27, 1993, <https://doi.org/10.3115/1072017.1072026>, 1993.

687 Coelho, J., Valente, M. T., Milen, L., and Silva, L. L.: Is this GitHub project maintained? Measuring the level of
688 maintenance activity of open-source projects, *Inf. Software Technol.*, 122, 106274,
689 <https://doi.org/10.1016/j.infsof.2020.106274>, 2020.

690 Comas, X., Wright, W., Hynek, S. A., Fletcher, R. C., and Brantley, S. L.: Understanding fracture distribution and
691 its relation to knickpoint evolution in the Rio Icacos watershed (Luquillo Critical Zone Observatory, Puerto Rico)
692 using landscape-scale hydrogeophysics, *Earth Surf. Processes Landforms*, 44(4), 877-885,
693 <https://doi.org/10.1002/esp.4540>, 2019.

694 Conrad, O., Bechtel, B., Bock, M., Dietrich, H., Fischer, E., Gerlitz, L., ... and Böhner, J.: System for automated
695 geoscientific analyses (SAGA) v. 2.1. 4, *Geosci. Model Dev.*, 8(7), 1991-2007, <https://doi.org/10.5194/gmd-8-1991-2015>, 2015.

697 Cresson, R.: A framework for remote sensing images processing using deep learning techniques, *IEEE Geosci.*
698 *Remote Sens. Lett.*, 16(1), 25-29, <https://doi.org/10.1109/lgrs.2018.2867949>, 2018.

699 Cresson, R. (2022). SR4RS: A tool for super resolution of remote sensing images, *J. Open Res. Software*, 10(1),
700 <https://doi.org/10.5334/jors.369>, 2022.

701 Cutler, A., Cutler, D. R., and Stevens, J. R.: Random forests, in: Ensemble machine learning: Methods and appli-
702 cations, edited by: Zhang, C., and Ma, Y., Springer, 157-175, https://doi.org/10.1007/978-1-4419-9326-7_5, 2012.

703 Dong, H., Peacor, D. R., and Murphy, S. F.: TEM study of progressive alteration of igneous biotite to kaolinite
704 throughout a weathered soil profile, *Geochim. Cosmochim. Acta*, 62(11), 1881-1887,
705 [https://doi.org/10.1016/s0016-7037\(98\)00096-9](https://doi.org/10.1016/s0016-7037(98)00096-9), 1998.

706 Elghali, A., Benzaazoua, M., Bouzazhah, H., Bussière, B., and Villarraga-Gómez, H.: Determination of the avail-
707 able acid-generating potential of waste rock, part I: Mineralogical approach, *Appl. Geochem.*, 99, 31-41,
708 <https://doi.org/10.1016/j.apgeochem.2018.12.010>, 2018

709 Fandrich, R., Gu, Y., Burrows, D., and Moeller, K.: Modern SEM-based mineral liberation analysis, *Int. J. Miner.*
710 *Process.*, 84(1-4), 310-320, <https://doi.org/10.1016/j.minpro.2006.07.018>, 2007.

711 Ferrier, K. L., Kirchner, J. W., Riebe, C. S., and Finkel, R. C.: Mineral-specific chemical weathering rates over
712 millennial timescales: Measurements at Rio Icacos, Puerto Rico, *Chem. Geol.*, 277(1-2), 101-114,
713 <https://doi.org/10.1016/j.chemgeo.2010.07.013>, 2010.

714 Fletcher, R. C., Buss, H. L., and Brantley, S. L.: A spheroidal weathering model coupling porewater chemistry to
715 soil thicknesses during steady-state denudation, *Earth Planet. Sci. Lett.*, 244(1-2), 444-457,
716 <https://doi.org/10.1016/j.epsl.2006.01.055>, 2006.

717 GDAL/OGR contributors: GDAL/OGR Geospatial Data Abstraction Software Library. Zenodo [code],
718 <https://doi.org/10.5281/zenodo.5884351>, 2023.

719 Gillies, S., and others: Rasterio: geospatial raster I/O for Python programmers, GitHub [code],
720 <https://github.com/rasterio/rasterio>, 2019.

721 Gillies, S., van der Wel, C., van den Bossche, J., Taves, M., Arnott, J., and Ward, B. C.: Shapely: Manipulation
722 and analysis of geometric objects in the Cartesian plane. Zenodo [code], <https://doi.org/10.5281/zenodo.5597138>,
723 2023.

724 Goldstein, J. I., Newbury, D. E., Michael, J. R., Ritchie, N. W., Scott, J. H. J., and Joy, D. C.: *Scanning Electron*
725 *Microscopy and X-ray Microanalysis*, 4th Edition, Springer, <https://doi.org/10.1007/978-1-4939-6676-9>, 2018.

726 Gonzalez, C. G., and Woods, R. E.: *Digital Image Processing*, 4th Edition, Pearson, 2018.

727 Goodfellow, B. W., and Hilley, G. E.: Climatic and lithological controls on the structure and thickness of granitic
728 weathering zones, *Earth Planet. Sci. Lett.*, 600, 117890, <https://doi.org/10.1016/j.epsl.2022.117890>, 2022.

729 Goodfellow, B. W., Hilley, G. E., Webb, S. M., Sklar, L. S., Moon, S., and Olson, C. A.: The chemical, mechani-
730 cal, and hydrological evolution of weathering granitoid, *J. Geophys. Res.: Earth Surf.*, 121(8), 1410-1435,
731 <https://doi.org/10.1002/2016jf003822>, 2016.

732 Gottlieb, P., Wilkie, G., Sutherland, D., Ho-Tun, E., Suthers, S., Perera, K., Jenkins, B., Spencer, S., Butcher, A.,
733 and Rayner, J.: Using quantitative electron microscopy for process mineralogy applications, *JOM*, 52, 24-25,
734 <https://doi.org/10.1007/s11837-000-0126-9>, 2000.

735 Grizonnet, M., Michel, J., Poughon, V., Inglada, J., Savinaud, M., and Cresson, R. (2017). Orfeo ToolBox: Open
736 source processing of remote sensing images, *Open Geospatial Data, Software and Stand.*, 2(1), 1-8,
737 <https://doi.org/10.1186/s40965-017-0031-6>, 2017.

738 Gu, Y. Automated scanning electron microscope based mineral liberation analysis. *Journal of Minerals and Mate-*
739 *rials Characterization and Engineering*, 2(1), <https://doi.org/10.4236/jmmce.2003.2100333-41>. 2003.

740 Guo, L., Chehata, N., Mallet, C., and Boukir, S.: Relevance of airborne lidar and multispectral image data for ur-
741 ban scene classification using Random Forests, *ISPRS J. Photogramm. Remote Sens.*, 66(1), 56-66,
742 <https://doi.org/10.1016/j.isprsjprs.2010.08.007>, 2011.

743 Han, S., Löhr, S. C., Abbott, A. N., Baldermann, A., Farkaš, J., McMahon, W., Miliken, K., Rafiei, M., Wheeler,
 744 C., and Owen, M.: Earth system science applications of next-generation SEM-EDS automated mineral mapping,
 745 Front. Earth Sci., 10, 956912, <https://doi.org/10.3389/feart.2022.956912>, 2022.

746 Harlov, D. E., Hansen, E. C., and Bigler, C.: Petrologic evidence for K-feldspar metasomatism in granulite facies
 747 rocks, Chem. Geol., 151(1-4), 373-386, [https://doi.org/10.1016/s0009-2541\(98\)00090-4](https://doi.org/10.1016/s0009-2541(98)00090-4), 1998.

748 Harris, C.R., Millman, K.J., van der Walt, S.J., Gommers, R., Virtanen, P., and Cournapeau, D.: Array program-
 749 ming with NumPy, Nature, 585, 357–362. <https://doi.org/10.1038/s41586-020-2649-2>, 2020.

750 Hazen, R. M., Papineau, D., Bleeker, W., Downs, R. T., Ferry, J. M., McCoy, T. J., and Yang, H.: Mineral evolu-
 751 tion, Am. Mineral., 93(11-12), 1693-1720, <https://doi.org/10.2138/am.2008.2955>, 2008.

752 He, H., & Garcia, E. A. Learning from imbalanced data. IEEE Transactions on knowledge and data engineering,
 753 21(9), 1263-1284, <https://doi.org/10.1109/TKDE.2008.239>, 2009.

754 Hilton, R. G., and West, A. J.: Mountains, erosion and the carbon cycle, Nat. Rev. Earth Environ., 1(6), 284-299,
 755 <https://doi.org/10.1038/s43017-020-0058-6>, 2020.

756 Hrstka, T., Gottlieb, P., Skala, R., Breiter, K., and Motl, D.: Automated mineralogy and petrology-applications of
 757 TESCANA Integrated Mineral Analyzer (TIMA), J. Geosci., 63(1), 47-63, <https://doi.org/10.3190/jgeosci.250>,
 758 2018.

759 Hupp, B. N., and Donovan, J. J.: Quantitative mineralogy for facies definition in the Marcellus Shale (Appala-
 760 chian Basin, USA) using XRD-XRF integration, Sediment. Geol., 371, 16-31,
 761 <https://doi.org/10.1016/j.sedgeo.2018.04.007>

762 Jordahl, K., Van den Bossche, J., Wasserman, J., McBride, J., Gerard, J., Fleischmann, M., ... and Greenhall, A.:
 763 geopandas/geopandas: v0.12.1, Zenodo [code], <https://doi.org/10.5281/zenodo.7262879>, 2022.

764 Keulen, N., Malkki, S. N., and Graham, S.: Automated quantitative mineralogy applied to metamorphic rocks,
 765 Minerals, 10(1), 47, <https://doi.org/10.3390/min10010047>, 2020.

766 Lanari, P., Vidal, O., De Andrade, V., Dubacq, B., Lewin, E., Grosch, E. G., and Schwartz, S.: XMapTools: A
 767 MATLAB©-based program for electron microprobe X-ray image processing and geothermobarometry, Comput.
 768 Geosci., 62, 227-240, <https://doi.org/10.1016/j.cageo.2013.08.010>, 2014.

769 Le Maitre, R. W.: Classification and nomenclature, in: *Igneous rocks: a classification and glossary of terms: rec-*
 770 *ommendations of the International Union of Geological Sciences Subcommission on the Systematics of Igneous*
 771 *Rocks*, edited by: Le Maitre, R. W., Streckeisen, A., Zanettin, B., Le Bas, M. J., Bonin, B., and Bateman, P.,
 772 Cambridge University Press, <https://doi.org/10.1017/CBO9780511535581>, 2002.

773 Li, C., Wang, D., and Kong, L.: Application of machine learning techniques in mineral classification for scanning
 774 electron microscopy-energy dispersive X-ray spectroscopy (SEM-EDS) images, J. Pet. Sci. Eng., 200, 108178,
 775 <https://doi.org/10.1016/j.petrol.2020.108178>, 2021.

776 Li, L., Lee, P. K. K., Tsui, Y., Tham, L. G., and Tang, C. A.: Failure process of granite, Int. J. Geomech., 3(1), 84-
 777 98, [https://doi.org/10.1061/\(ASCE\)1532-3641\(2003\)3:1\(84\)](https://doi.org/10.1061/(ASCE)1532-3641(2003)3:1(84)), 2003.

778 Mahabadi, O. K., Randall, N. X., Zong, Z., and Grasselli, G.: A novel approach for micro-scale characterization
 779 and modeling of geomaterials incorporating actual material heterogeneity, *Geophys. Res. Lett.*, 39(1),
 780 <https://doi.org/10.1029/2011gl050411>, 2012.

781 Malac, M., Calzada, J. A. M., Salomons, M., Homeniuk, D., Price, P., Cloutier, M., ... and Egerton, R.: NanoMi:
 782 An open source electron microscope hardware and software platform, *Micron*, 163, 103362,
 783 <https://doi.org/10.1016/j.micron.2022.103362>, 2022.

784 Marra, W. A., van de Grint, L., Alberti, K., and Karssenberg, D. : Using GIS in an Earth Sciences field course for
 785 quantitative exploration, data management and digital mapping, *J. Geogr. Higher Educ.*, 41(2), 213-229,
 786 <https://doi.org/10.1080/03098265.2017.1291587>, 2017.

787 Maxwell, A. E., Warner, T. A., and Fang, F.: Implementation of machine-learning classification in remote sensing:
 788 An applied review, *Int. J. Remote Sens.*, 39(9), 2784-2817, <https://doi.org/10.1080/01431161.2018.1433343>,
 789 2018.

790 McInerney, D., and Kempeneers, P.: Virtual Rasters and Raster Calculations. in: *Open Source Geospatial Tools:*
 791 *Applications in Earth Observation, Earth Systems Data and Models.* Springer, [https://doi.org/10.1007/978-3-319-](https://doi.org/10.1007/978-3-319-01824-9_11)
 792 [01824-9_11](https://doi.org/10.1007/978-3-319-01824-9_11), 2015.

793 Murphy, S. F., Brantley, S. L., Blum, A. E., White, A. F., and Dong, H.: Chemical weathering in a tropical water-
 794 shed, Luquillo Mountains, Puerto Rico: II. Rate and mechanism of biotite weathering, *Geochim. Cosmochim.*
 795 *Acta*, 62(2), 227-243, [https://doi.org/10.1016/s0016-7037\(97\)00336-0](https://doi.org/10.1016/s0016-7037(97)00336-0), 1998.

796 Newbury, D. E., and Ritchie, N. W.: Elemental mapping of microstructures by scanning electron microscopy-en-
 797 ergy dispersive X-ray spectrometry (SEM-EDS): extraordinary advances with the silicon drift detector (SDD), *J.*
 798 *Anal. At. Spectrom.*, 28(7), 973-988, <https://doi.org/10.1039/c3ja50026h>, 2013.

799 Nikonow, W., and Rammlmair, D.: Automated mineralogy based on micro-energy-dispersive X-ray fluorescence
 800 microscopy (μ -EDXRF) applied to plutonic rock thin sections in comparison to a mineral liberation analyzer, *Ge-*
 801 *osci. Instrum. Methods Data Syst.*, 6(2), 429-437, <https://doi.org/10.5194/gi-6-429-2017>, 2017.

802 Nikonow, W., Rammlmair, D., Meima, J. A., and Schodlok, M. C.: Advanced mineral characterization and petro-
 803 graphic analysis by μ -EDXRF, LIBS, HSI and hyperspectral data merging, *Mineral. Petrol.*, 113, 417-431,
 804 <https://doi.org/10.1007/s00710-019-00657-z>, 2019.

805 Orlando, J., Comas, X., Hynek, S. A., Buss, H. L., and Brantley, S. L.: Architecture of the deep critical zone in
 806 the Río Icacos watershed (Luquillo Critical Zone Observatory, Puerto Rico) inferred from drilling and ground
 807 penetrating radar (GPR), *Earth Surf. Processes Landforms*, 41(13), 1826-1840, <https://doi.org/10.1002/esp.3948>,
 808 2016.

809 Ortolano, G., Visalli, R., Godard, G., and Cirrincione, R.: Quantitative X-ray Map Analyser (Q-XRMA): A new
 810 GIS-based statistical approach to Mineral Image Analysis, *Comput. Geosci.*, 115, 56-65,
 811 <https://doi.org/10.1016/j.cageo.2018.03.001>, 2018.

812 Ortolano, G., Zappalà, L., and Mazzoleni, P.: X-Ray Map Analyser: A new ArcGIS® based tool for the quantita-
813 tive statistical data handling of X-ray maps (Geo-and material-science applications), *Comput. Geosci.*, 72, 49-64,
814 <https://doi.org/10.1016/j.cageo.2014.07.006>, 2014.

815 Pedregosa, F., Varoquaux, G., Gramfort, A., Michel, V., Thirion, B., Grisel, O., ... and Duchesnay, É.: Scikit-
816 learn: Machine learning in Python, *J. Mach. Learn. Res.*, 12, 2825-2830,
817 <https://doi.org/10.48550/arxiv.1201.0490>, 2011.

818 Perkins, D.: Mineralogy, Open Educational Resources, University of North Dakota,
819 <https://doi.org/10.31356/oers025>, 2020.

820 Pirrie, D., and Rollinson, G. K.: Unlocking the applications of automated mineral analysis, *Geol. Today*, 27(6),
821 226-235, <https://doi.org/10.1111/j.1365-2451.2011.00818.x>, 2011.

822 Přikryl, R.: Assessment of rock geomechanical quality by quantitative rock fabric coefficients: limitations and
823 possible source of misinterpretations, *Eng. Geol.*, 87(3-4), 149-162,
824 <https://doi.org/10.1016/j.enggeo.2006.05.011>, 2006.

825 Probst, P., Wright, M. N., and Boulesteix, A. L.: Hyperparameters and tuning strategies for random forest, *Wiley*
826 *Interdiscip. Rev.: Data Min. Knowl. Discovery*, 9(3), e1301, <https://doi.org/10.1002/widm.1301>, 2019.

827 Rafiei, M., Löhr, S., Baldermann, A., Webster, R., and Kong, C.: Quantitative petrographic differentiation of de-
828 trital vs diagenetic clay minerals in marine sedimentary sequences: Implications for the rise of biotic soils, *Pre-*
829 *cambrian Research*, 350, 105948, <https://doi.org/10.1016/j.precamres.2020.105948>, 2020.

830 Ramachandran, R., Bugbee, K., and Murphy, K.: From open data to open science, *Earth Space Sci.*, 8(5),
831 e2020EA001562, <https://doi.org/10.1029/2020EA001562>, 2021.

832 Raza, A., and Capretz, L. F.: Contributors preference in open source software usability: An empirical study, *arXiv*
833 [preprint], <https://doi.org/10.48550/arXiv.1507.06882>, 24 July 2015.

834 Riebe, C. S., Kirchner, J. W., and Finkel, R. C.: Long-term rates of chemical weathering and physical erosion
835 from cosmogenic nuclides and geochemical mass balance, *Geochim. Cosmochim. Acta*, 67(22), 4411-4427,
836 [https://doi.org/10.1016/s0016-7037\(03\)00382-x](https://doi.org/10.1016/s0016-7037(03)00382-x), 2003.

837 Reed, M. M., Ferrier, K. L., Nachlas, W. O., Schneider, B., Arson, C., Xu, T., Shen, X., West, N.: Supplement to
838 “A free, open-source method for automated mapping of quantitative mineralogy from energy-dispersive X-ray
839 spectroscopy scans of rock thin sections”, *Zenodo* [code and datasets], <https://doi.org/10.5281/zenodo.10912628>,
840 2024.

841 Schulz, B., Sandmann, D., and Gilbricht, S.: SEM-based automated mineralogy and its application in geo-and
842 material sciences, *Minerals*, 10(11), 1004, <https://doi.org/10.3390/min10111004>, 2020.

843 Shen, X., Arson, C., Ferrier, K. L., West, N., and Dai, S.: Mineral weathering and bedrock weakening: Modeling
844 microscale bedrock damage under biotite weathering, *J. Geophys. Res.: Earth Surf.*, 124(11), 2623-2646,
845 <https://doi.org/10.1029/2019jf005068>, 2019.

846 Speer, J. A. (1984). Micas in igneous rocks, *Rev. Mineral. Geochem.*, 13(1), 299-356.

847 Stallard, R. F., and Murphy, S. F.: Water quality and mass transport in four watersheds in eastern Puerto Rico.
 848 Water quality and landscape processes of four watersheds in eastern Puerto Rico. US Geol. Surv. Prof. Pap.,
 849 1789, 113-152. <https://doi.org/10.3133/pp1789E>, 2012.

850 Sutherland, D., Gottlieb, P., Jackson, R., Wilkie, G., & Stewart, P. Measurement in section of particles of known
 851 composition. Minerals Engineering, 1(4), 317-326, [https://doi.org/10.1016/0892-6875\(88\)90021-0](https://doi.org/10.1016/0892-6875(88)90021-0), 1988.

852 Sutherland, D. N., and Gottlieb, P. Application of automated quantitative mineralogy in mineral processing. Min-
 853 erals Engineering, 4(7-11), 753-762, [https://doi.org/10.1016/0892-6875\(91\)90063-2](https://doi.org/10.1016/0892-6875(91)90063-2), 1991.

854 Tapponnier, P., and Brace, W. F.: Development of stress-induced microcracks in Westerly granite. In: Interna-
 855 tional Journal of Rock Mechanics and Mining Sciences & Geomechanics Abstracts, [https://doi.org/10.1016/0148-](https://doi.org/10.1016/0148-9062(76)91937-9)
 856 [9062\(76\)91937-9](https://doi.org/10.1016/0148-9062(76)91937-9), 1976.

857 Tarquini, S., and Favalli, M.: A microscopic information system (MIS) for petrographic analysis, Comput. Ge-
 858 osci., 36(5), 665-674, <https://doi.org/10.1016/j.cageo.2009.09.017>, 2010.

859 Ündül, Ö.: Assessment of mineralogical and petrographic factors affecting petro-physical properties, strength and
 860 cracking processes of volcanic rocks, Eng. Geol., 210, 10-22, <https://doi.org/10.1016/j.enggeo.2016.06.001>,
 861 2016.

862 Wahrhaftig, C.: Stepped topography of the southern Sierra Nevada, California, Geol. Soc. Am. Bull., 76(10),
 863 1165-1190, [https://doi.org/10.1130/0016-7606\(1965\)76\[1165:stotss\]2.0.co;2](https://doi.org/10.1130/0016-7606(1965)76[1165:stotss]2.0.co;2), 1965.

864 White, A. F., Blum, A. E., Schulz, M. S., Vivit, D. V., Stonestrom, D. A., Larsen, M., Murphy, S., and Eberl, D.:
 865 Chemical weathering in a tropical watershed, Luquillo Mountains, Puerto Rico: I. Long-term versus short-term
 866 weathering fluxes, Geochim. Cosmochim. Acta, 62(2), 209-226, [https://doi.org/10.1016/s0016-7037\(97\)00335-9](https://doi.org/10.1016/s0016-7037(97)00335-9),
 867 1998.

868 Xu, T., Shen, X., Reed, M., West, N., Ferrier, K. L., and Arson, C.: Anisotropy and microcrack propagation in-
 869 duced by weathering, regional stresses and topographic stresses, J. Geophys. Res.: Solid Earth, 127(7),
 870 e2022JB024518, <https://doi.org/10.1029/2022JB024518>, 2022.

871